



Customized design of nZVI supported on an N-doped reduced graphene oxide aerogel for microwave-assisted superefficient degradation of imidacloprid in wastewater

Peng Zhang^{a,b}, Xingying Meng^{a,b,1}, Mingyi Fan^{a,b,1}, Sai Wu^{a,b}, Cuiping Wang^{a,b}, Xiaofu Shang^c, Hanzhong Jia^d, Hongwen Sun^{a,b,*}

^a MOE Key Laboratory of Pollution Processes and Environmental Criteria, College of Environmental Science and Engineering, Nankai University, Tianjin 300350, China

^b Tianjin Engineering Center of Environmental Diagnosis and Contamination Remediation, Tianjin 300350, China

^c Tianjin Academy of Environmental Science, Tianjin 300350, China

^d College of Natural Resources and Environment, Northwest A&F University, Yangling, Shaanxi Province 712100, China

ARTICLE INFO

Keywords:

Microwave irradiation
Reduced graphene oxide
nZVI
Catalytic degradation
Advanced wastewater treatment

ABSTRACT

High-performance and energy-saving microwave (MW)-assisted catalysts are of great significance for MW-assisted treatments of wastewater. Herein, a novel nitrogen-doped reduced graphene oxide aerogel with supported nanoscale zero-valent iron (nZVI@N-rGOA) was successfully synthesized and used in the MW-assisted removal of imidacloprid (IMI) from wastewater. The resulting nZVI@N-rGOA had an open pomegranate-like multicompartiment structure consisting of wrinkled flaky reticular N-rGOA walls and embedded nZVI particles, and the nZVI@N-rGOA/MW system rapidly eliminated nearly 100% of the IMI in a 10 mg/L solution within 2 min. The highly efficient MW-assisted catalytic degradation of IMI resulted from synergistic effects, including the nZVI active centres, pyridinic N sites and open pomegranate-like multicompartiment structures, which facilitated MW harvesting, mass transfer of the reactants and generation of heat, electrons, holes and $\bullet\text{OH}$ radicals. Accordingly, the localized surface plasmon resonance and electron transfer processes enabled catalytic oxidations/reductions, respectively. This work provides a novel paradigm for designing MW-assisted catalysts for wastewater treatment.

1. Introduction

With the rapid development of industrialization and the economy and the continuous progress of human society, the amount of organic wastewater generated by various industries has increased continuously, which places great pressure on the survival of human beings and restricts future development [1,2]. In the development of efficient pollutant purification technologies, catalytic purification of organic pollutants has become key; it features low ignition temperatures, fast reactions, high treatment efficiencies and directional transformation of pollutants, and has been an important issue in wastewater treatment studies in recent years [3].

Microwaves (MWs) are electromagnetic waves with frequencies of 0.3–300 GHz and wavelengths of 0.001–1 m, and they have advantages noncontact selective, volumetric and uniform heating without

temperature gradients for MW-absorbing materials [4,5]. In recent years, MW-assisted wastewater treatment technology has shown good application prospects in the field of organic wastewater treatment and has received attention from many researchers [6]. MW-assisted catalysts (e.g., activated carbon, graphene and transition metal oxides) absorb and convert MW energy into heat that causes rapid temperature increases within the materials [7]. Compared with conventional heating system in which heat diffuses from the surface of the material to the interior, the thermal effect of MW irradiation is rapidly produced within the material, so the internal temperature is greater than that of the surface [8]. Additionally, the material surface has active “hot spots” and microplasmas, which provide active species, e.g., free electrons, $\bullet\text{OH}$, $\bullet\text{O}_2$ and holes, that degrade organic pollutants [5,9]. In general, MW-assisted treatment greatly improves the disposal process of conventional heating with short treatment times and high efficiencies in

* Correspondence to: Nankai University, 38# Tongyan Road, Haihe Education Park, Jinnan District, Tianjin 300350, China.

E-mail address: sunhongwen@nankai.edu.cn (H. Sun).

¹ Xingying Meng and Mingyi Fan contributed equally to this paper.

catalytic degradation of organic pollutants, and it saves energy and reduces consumption [10].

Iron-based materials (e.g., zero-valent iron (ZVI), iron minerals) are the most commonly used metallic catalysts for MW-assisted catalytic oxidation systems due to their environmentally friendly natures and natural abundance [11,12]. Among them, nano ZVI (nZVI) exhibits high conductivity and extremely high eddy current losses and magnetic resonance losses [13], and it adsorbs MW energy and generates a ring electric current to form an oscillating electric field with charge carriers, thus generating internal heat in the material and a microplasma region that generates electron-hole pairs on the material surface during catalytic degradation of pollutants [14]. However, the electron-hole pairs recombine rapidly, so the thermal effect is far less than that of water [15]. MW irradiation and sharply rising water temperatures excite water molecules to greater vibrational and rotational energy levels and weaken hydrogen bonds, which is conducive to oxygen absorption corrosion of the nZVI and generation of the byproducts H_2 and Fe^{2+} [5]. This also means that the utilization rate for nZVI electrons in catalytic degradation of organic pollutants is greatly constrained under MW irradiation. Thus, there is a need for customized nZVI-based catalysts to achieve efficient MW harvesting, high electron utilization rates and rapid degradation of organics.

Carbonaceous materials have excellent MW-absorbing properties and are widely used in MW-assisted catalytic oxidations of organic pollutants in environmental purification processes [8]. Among them, N-doped reduced graphene oxide aerogels (N-rGOAs) have attracted great attention due to their unique chemical and physical properties [16]. In particular, the three-dimensional network, abundant interfaces and surface functionalities, uneven charge distributions and developed pore structure offer rich void spaces enabling effective absorption of MW radiation, high electron mobility, stability of the internal nZVI and highly selective adsorption of organic pollutants [17–19]. Many studies have confirmed efficient MW harvesting and the finite catalytic activity of carbonaceous materials in pollutant degradation [20]. However, single carbonaceous materials, such as N-rGOA, exhibiting high dielectric loss and low magnetic loss cannot harvest MWs efficiently, so they exhibit low catalytic activities [21]. Recently, composite catalysts comprising carbonaceous and metallic materials (e.g., FeO , Fe_3O_4 and $CoFe_2O_4$) have received growing interest because of their synergistic catalytic effects and MW-absorption capacities, which enhance pollutant degradation and exhibit low cost and easy recovery [11,22]. Since they combine the merits of N-rGOA with nZVI, it is clear that nZVI/N-rGOA composites should exhibit superior MW absorption and catalytic activities. To our knowledge, research on the effects of N doping and nZVI loading on the dielectric and magnetic losses, MW absorption, catalytic performance and mechanisms for treatment of organic pollutants by nZVI@N-rGOA and MW irradiation has rarely been reported, and more effort is required.

Herein, we prepared a novel MW-assisted nZVI@N-rGOA composite catalyst with a well-designed three-dimensional porous and entangled structure and great dielectric and magnetic losses by loading nZVI on N-doped rGOA, and we coupled this catalyst with MW irradiation for efficient degradation of the typical pesticides found in wastewater. Imidacloprid (IMI) was selected as the target organic pollutant due to its high water solubility, potential leaching risk, recalcitrant chemical structure, prevalence as one of the most widely used insecticides, and adverse effects on nontarget organisms such as pollinators and birds. The objectives of this study were to (i) design and synthesize a novel nZVI@N-rGOA catalyst and analyse the microstructure and dielectric and magnetic losses to optimize MW absorption and MW-assisted and efficient degradation of organic pollutants; (ii) evaluate the MW-induced thermal and nonthermal effects for nZVI@N-rGOA-catalysed removal of organic pollutants by formation of various active species; and (iii) clarify the synergistic effect and mechanism of N-doped rGOA, nZVI and MW irradiation in an MW-assisted nZVI@N-rGOA catalytic degradation system. The results of this study will facilitate the design of

superefficient, sustainable, and eco-friendly engineered ZVI-carbon composite catalysts for use in MW-assisted wastewater treatment.

2. Materials and Methods

2.1. Chemicals

Detailed information on the chemicals used in this study is provide in Text S1 of the [Supporting Information](#) (SI). A stock solution of 500 mg/L IMI was prepared with deionized water and stored at 4 °C for the subsequent degradation experiments.

2.2. Preparation and characterization of the nZVI@N-rGOA composite

2.2.1. rGOA and N-rGOA syntheses

rGOA was synthesized according to our previous method [18], and the detailed procedure is shown in Text S2. Melamine (1.0 g) was added to a 1.67 g/L as-synthesized rGOA suspension and stirred for 12 h to reach adsorption equilibrium. Then, the solid was collected via centrifugation and freeze-dried for 48 h. The dried solid was placed in an atmosphere furnace and pyrolyzed at 350 °C for 60 min under a N_2 atmosphere with a heating rate of 5 °C min^{-1} . The resultant N-rGOA was washed with 500 mL of deionized water to remove the residual melamine and then freeze-dried for 48 h.

2.2.2. Syntheses of nZVI@rGOA and nZVI@N-rGOA composites

A total of 1.0 g of the as-synthesized rGOA or N-rGOA was dispersed in 500 mL of deionized water with stirring. The suspension was mixed with 25.0 g of a $FeSO_4 \cdot 7 H_2O$ solution in a three-neck flask and continuously stirred under a N_2 atmosphere for 6 h. Fifty millilitres of a 5 M $NaBH_4$ solution was added to the mixtures and stirred for 30 min. The collected products were rinsed with deionized water and freeze-dried for 48 h. The obtained solids were labelled nZVI@rGOA and nZVI@N-rGOA.

2.2.3. Characterization

The detailed characterization data for the nZVI@N-rGOA composite is provided in Text S3, including scanning electron microscopy (SEM) images, X-ray diffraction (XRD) data, X-ray photoelectron spectra (XPS), Fourier transform infrared spectra (FTIR), Fe contents in the composites, H_2 production rates, reflection losses (RLs) and magnetic hysteresis loops.

2.3. Degradation experiments

Batch degradation experiments of IMI were performed in a temperature-controlled MW reactor (MW frequency: 2.45 GHz; MCR-3, Kerui Instrument Company, China) with an operating power of 900 W and irradiation with continuous mechanical stirring. The catalytic process was conducted in a 100 mL glass flask with a 25 mL suspension containing 100–400 mg/L IMI and a 0.5 g/L catalyst solution. The pH values of the suspensions were 7.0 ± 0.2 and were not adjusted. Boiling and rapid evaporation of the water was avoided during the experiment, and unless otherwise specified, the maximum temperature for the catalytic suspension was maintained at 90 °C with a temperature-controlled MW reactor. At selected reaction times, 1.0 mL suspensions were withdrawn and filtered through a 0.22- μm filter membrane. Then, 0.5 mL of the filtrate was put into a 2.0-mL sampling vial and stored at 4 °C for further concentration and analyses of the IMI degradation intermediates and products (Text S4, SI). Each experiment was carried out in duplicate. Traditional heat treatment (oil bath) served as a control experiment, and the procedure was similar to those of the batch degradation experiments. During the process, the water temperature and MW power curves of the MW-assisted systems were documented.

The effects of pH (1–11), cations (Na^+ , Mg^{2+}) and anions (HCO_3^- , NO_3^- , $H_2PO_4^-$) on IMI catalytic degradation were determined with the

MW-assisted catalytic system. In the recycling experiments, nZVI@N-rGOA was collected via magnetic separation, mixed with the NaBH₄ solution and stirred for 30 min. The solids were rinsed with deionized water, freeze-dried for 48 h, and then stored at −20 °C for the subsequent recycling experiments.

Electron paramagnetic resonance (EPR, Bruker E500, Germany) was used to determine the active species (e.g., reactive oxide species (ROS) and electrons) present in the MV-assisted catalytic system. The radical signals were trapped with 2,2,6,6-tetramethyl-4-piperidone (TEMP) and 5,5-dimethyl-1-pyrroline-N-oxide (DMPO), the electrons in solution were trapped with 2,2,6,6-tetramethylpiperidine-1-oxyl (TEMPO), and the EPR spectra were obtained at 25 °C. To identify the contributions of ROS to IMI degradation, designed amounts of various scavengers (tert-butyl alcohol (TBA) for ·OH, chloroform (CF) for O₂^{·−}, *p*-benzoquinone (*p*-BQ) for electrons and O₂^{·−}, triethylenediamine (DABCO) for ¹O₂, and KI for holes (h⁺)) were added to the nZVI@N-rGOA/WM system during IMI removal.

2.4. Statistical analyses

The degradation kinetics of IMI were calculated with the following equations: $\ln(C_t/C_0) = -K_{obs}t$, where C_0 and C_t are the IMI concentrations at 0 and time t , respectively, K_{obs} (min^{−1}) is the degradation rate constant, and t (min) is the reaction time.

The synergetic effect of MW irradiation, nZVI, N-doping and rGOA

on IMI catalytic degradation was evaluated with the synergetic index [20]: $\text{synergetic index} = k/(k_1 + k_2 + k_3)$, where k , k_1 , k_2 , and k_3 represent the rate constants in the reactions of nZVI@N-rGOA/WM, nZVI/WM, N-rGOA/WM and rGOA/WM, respectively.

3. Results and Discussion

3.1. Structural analyses

As presented in Fig. 1a, the diffraction peaks at 44.8° in the XRD patterns of nZVI, nZVI@rGOA and nZVI@N-rGOA corresponded to the (110) crystalline plane of Fe⁰ (JCPDS No. 06-0696) [23]. However, the intensities of the diffraction peaks for Fe⁰ in the patterns for nZVI@N-rGOA were lower than those for nZVI, which suggested a disordered structure and loss of crystallinity for the nZVI in nZVI@N-rGOA.

The SEM images (Fig. 1b–c) showed that rGOA displayed a 3D interconnected structure consisting of wrinkled and coalesced nanoscale graphene sheets, and N-doping enhanced the number of wrinkled and flaky graphene sheets, increased the special surface area (SSA) and pore volume (Table S1), and formed open reticular walls of N-rGOA. These folds, holes and cracks provided abundant anchor and adhesion sites for nZVI particles when rGOA and N-rGOA were introduced as carbon carriers in the synthesis of nZVI (Fig. 1d–e). In particular, nZVI@N-rGOA had an open pomegranate-like multicompartiment structure consisting

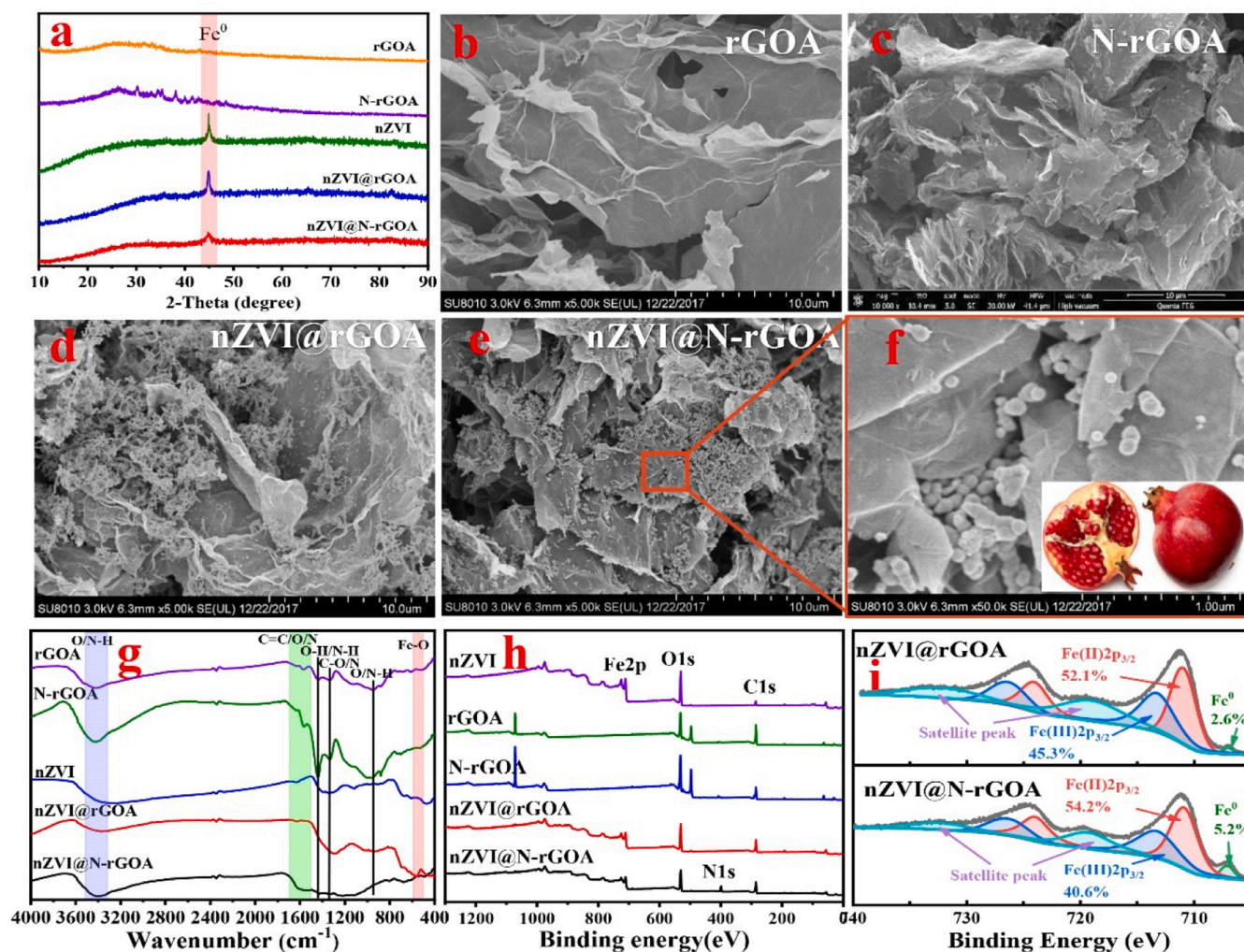


Fig. 1. XRD patterns (a) and SEM images of rGOA (b), N-rGOA (c), nZVI@rGOA (d) and nZVI@N-rGOA (e, f), FTIR spectra (g), wide-scan XPS spectrum (h) and high-resolution Fe 2p XPS spectra of nZVI@N-rGOA (i).

of wrinkled flaky reticular N-rGOA walls and embedded nZVI particles (Fig. 1e-f). Furthermore, nZVI@N-rGOA presented a more compact structure than nZVI@rGOA, and more of the nZVI was surrounded by flaky N-rGOA. The 51.8 and 58.3 wt% Fe contents in nZVI@rGOA and nZVI@N-rGOA were verified by inductively coupled plasma optical emission spectroscopy. This suggested that the N-doping sites were involved in nZVI loading. This was also observed in previous studies [19] and demonstrated that the N-doping sites provided lower negative potentials, more bond structures and Lewis basic sites in the carbon network [19,24] and facilitated anchoring and adhesion of nZVI on the N-rGOA. Furthermore, the TEM images of nZVI@N-rGOA (Fig. S1) confirmed that the surface of N-rGOA was full of wrinkles, and the nZVI particles were present in the interior of the N-rGOA, which was consistent with the SEM images (Fig. 1e-f).

The FTIR spectra of the as-prepared catalysts are shown in Fig. 1g. The broad bands at 3421, 1438 and 950 cm^{-1} corresponded to O-H/N-H, and the peaks appearing at 1640, 1570 and 1330 cm^{-1} were attributed to C=C/O/N vibrations and the stretching vibrations of C-C/O/N species. The intensities of these peaks were enhanced by N doping. This confirmed that N atoms were successfully introduced into the carbon network of the rGOA. Additionally, the peaks for nZVI, nZVI@rGOA and nZVI@N-rGOA at 568 and 665 cm^{-1} arose from Fe-O stretching vibrations [25]. However, loading nZVI on rGOA and N-rGOA weakened the intensity of the O-H/N-H, C=C/O/N, and C-C/O/N peaks due to bonding between the O- and N-containing functional groups (OFGs, NFGs) and nZVI via complexation and coordination on the surfaces of these composites.

Subsequently, the surface elemental composition and chemical states of nZVI@N-rGOA were determined by XPS. The wide scan and high-resolution C 1s and N 1s XPS spectra for nZVI@N-rGOA (Fig. 1h and S2) reconfirmed the presence of the OFGs (e.g., O-C=O, C=O, C-O) and NFGs (e.g., graphitic N, pyrrolic N and pyridinic N) and suggested that N atoms were successfully doped into the carbon network structure of rGOA and replaced some of the original C positions. Furthermore, the electrostatic potential maps (Fig. S3) revealed that the N-doping process generated defects, structural disorder or carbon edge termination in the graphite network, and the N-doping sites modulated the electronic structures of the adjacent C atoms. Specifically, the electrostatic potentials of the pyrrolic N and pyridinic N were more negative, which

facilitated anchoring and adhesion of nZVI on N-rGOA [26]. Furthermore, after N-doping, N-rGOA was more hydrophobic than rGOA (Fig. S4), suggesting a higher absorption capacity for organic pollutants. As shown in Fig. 1i, the peaks at 707.2, 710.6, 712.3 and 720.0 eV were attributed to Fe 2p_{1/2} (Fe⁰), Fe 2p_{3/2} (Fe(II)), Fe 2p_{3/2} (Fe(III)) binding energies and satellite peaks, respectively, which are the fingerprints of nZVI [27,28]. Moreover, the Fe(II) and Fe(III) peaks appeared in the spectra of nZVI@N-rGOA and nZVI@rGOA before they were used as MW-assisted catalysts, indicating that the nZVI in nZVI@N-rGOA and nZVI@rGOA was oxidized to form thin oxide layers on the surfaces. However, in comparison with nZVI@rGOA, nZVI@N-rGOA showed lower proportions of Fe(III), which was due to the compact pomegranate-like multicompartiment structures of nZVI@N-rGOA, which protected nZVI from oxidation by oxygen.

3.2. Electromagnetic characteristics of the catalysts

To investigate the electromagnetic parameters and MW absorption capacities of the synthesized catalysts, contour maps showing the reflection losses (RLs) in the frequency range 1.0–6.0 GHz were generated. As shown in Fig. 2a, pure nZVI, rGOA, N-rGOA and their composites exhibited different sensitivities to MW irradiation. For rGOA and N-rGOA, the minimum RLs were −9.8 and −13.4 dB, respectively. Notably, N-rGOA showed a broad absorption bandwidth at 1.8–2.8 GHz. As carbonaceous MW-adsorbing materials, rGOA and N-rGOA exhibited high dielectric losses and activities, which are highly dependent on the graphitization degree, morphological structure, residual defects and surface functionality [31]. Our study also suggested that N-rGOA, the best-performing MW adsorbent, had a 3D pomegranate-like multicompartiment structure consisting of wrinkled reticular walls with abundant pores (Fig. 1 and Table S1). When they penetrated the inner spaces of the N-rGOA, the MWs were restricted and rarely escaped from the absorber; pores and multiple reflections were formed, and the incident MW was scattered (Fig. 2b), while the many open reticular pores induced multiple sites of interfacial polarization and eddy currents (Fig. 2c), increased the MW propagation paths and exhausted the MW energy via intrinsic dielectric and conduction loss from N-rGOA [32]. Additionally, electron-rich pyrrolic N and pyridinic N structures, and especially pyridinic N with its lone pair electrons (Fig. S3), generated

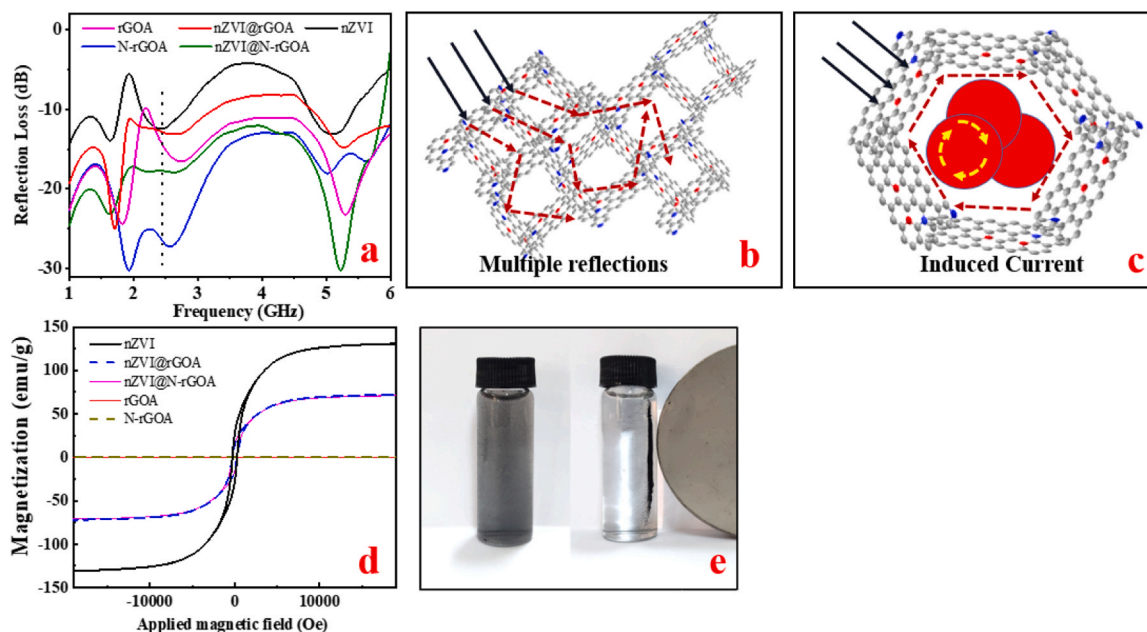


Fig. 2. Reflection loss (RL) curves (a), multiple interface reflections (b), induced current mechanism (c), magnetic hysteresis loops (d) and magnetic separation picture (e) of the as-synthesized catalysts.

dielectric losses, whereas the graphitic N generated conduction losses [22]. It can be concluded that N-doping improved the dielectric and conduction losses and broad bandwidths of the N-rGOA. Meanwhile, the nZVI generated a minimum RL of only -4.2 dB, which indicated ineffective MW absorption over the frequency range 1.0 – 6.0 GHz due to magnetic losses (mainly eddy current losses). However, it is obvious that MW absorption was markedly enhanced by the combination of N-rGOA with nZVI, and a broad effective absorption band was seen at 1.0 – 5.5 GHz ($RL < -12.1$ dB). In particular, at 2.45 GHz (the MW frequency used in this study), nZVI@N-rGOA exhibited efficient MW absorption and a low RL of -24.4 dB. The strong MW absorption by nZVI@N-rGOA may be due to its unique 3D pomegranate-like multi-compartment structure with abundant N-doped sites and pores and the dielectric, conduction and magnetic losses; these enable efficient MW adsorption due to the multiple reflections and scattering of the incident MWs, dielectric and conduction losses of N-rGOA and magnetic losses of nZVI [32].

The magnetic hysteresis loops of nZVI, rGOA, N-rGOA and nZVI@N-rGOA are illustrated in Fig. 2d. Owing to their nonmagnetic natures, rGOA and N-rGOA presented saturation magnetizations of almost 0, while the saturation magnetizations of nZVI and nZVI@N-rGOA were 131.1 and 71.1 emu/g, respectively. This suggested that nZVI@N-rGOA would be highly susceptible to magnetic separation and rapid collection from water bodies (Fig. 2e). Furthermore, numerous previous studies have illustrated that MW absorption depends on the magnetic and dielectric loss factors of the targeted material [5,33]. Compared with nZVI (pure magnetic loss material) and N-rGOA (pure dielectric/conduction loss material), nZVI@N-rGOA exhibited much larger magnetic and dielectric loss factors and thus has a clear advantage in MW absorption due to the various magnetic/dielectric/conduction losses. Thus, based on the above analysis, the excellent electromagnetic characteristics of nZVI@N-rGOA can be attributed to the synergistic effects of nZVI and N-rGOA.

3.3. Catalytic reactivity

The kinetics for removal of IMI by various catalysts under different reaction conditions (e.g., room temperature, MW irradiation, and traditional heating in an oil bath) are compared in Fig. 3a–c. As shown in Fig. 3a, the efficiencies for removal of IMI within 16 min by various catalysts at room temperature were all lower than 26.5%, which was a result of adsorption [34] and reduction degradation [35]. The significantly enhanced IMI removal under MW irradiation was also clear from the results presented in Fig. 3c, and the removal percentages of IMI at the end of the reaction (7 min) decreased in the order nZVI@N-rGOA/MW > nZVI@rGOA/MW > nZVI/MW > N-rGOA/MW > rGOA/MW. Rapid removal of IMI was achieved, with a removal rate of nearly 100% within 2 min for nZVI@N-rGOA/MW. Correspondingly, the removal rate constants (k) of nZVI@N-rGOA/MW, nZVI@rGOA/MW, nZVI/MW, N-rGOA/MW and rGOA/MW were 2.74 , 0.24 , 0.20 , 0.17 and 0.13 min^{-1} , respectively (Fig. 3d). This indicated that the combination of nZVI and N-rGOA produced a synergistic effect for nZVI@N-rGOA/MW-catalysed removal of IMI. Based on the low IMI removal efficiency caused by adsorption, the efficient removal of IMI by the catalyst/MW system was primarily caused by degradation. To evaluate the synergistic effect, the synergistic index was calculated (Fig. 3d). The synergistic index was 3.66 , i.e., 266% more efficient than nZVI/MW, rGOA/MW, N-rGOA/MW and nZVI@rGOA/MW combined. This confirmed positive coupling of the nZVI and N-rGOA for MW-assisted catalytic removal of IMI, as discussed below. Furthermore, compared to other reported carbonaceous and metallic MW-assisted materials used in previous studies (e.g., porous/activated carbon, carbon nanotubes, and nZVI@graphene) (Table S2), nZVI@N-rGOA/MW exhibited a greater catalytic capacity and quicker removal of IMI. Additionally, the kinetics for the removal of different initial IMI concentrations (100 – 400 mg/L) by nZVI@N-rGOA/WM (Fig. S5) showed that less than 200 mg/L of IMI was completely removed within 2 min, and the IMI removal rate decreased with increasing IMI concentrations from 200 mg/L to 400 mg/L. This may be attributed to an insufficient

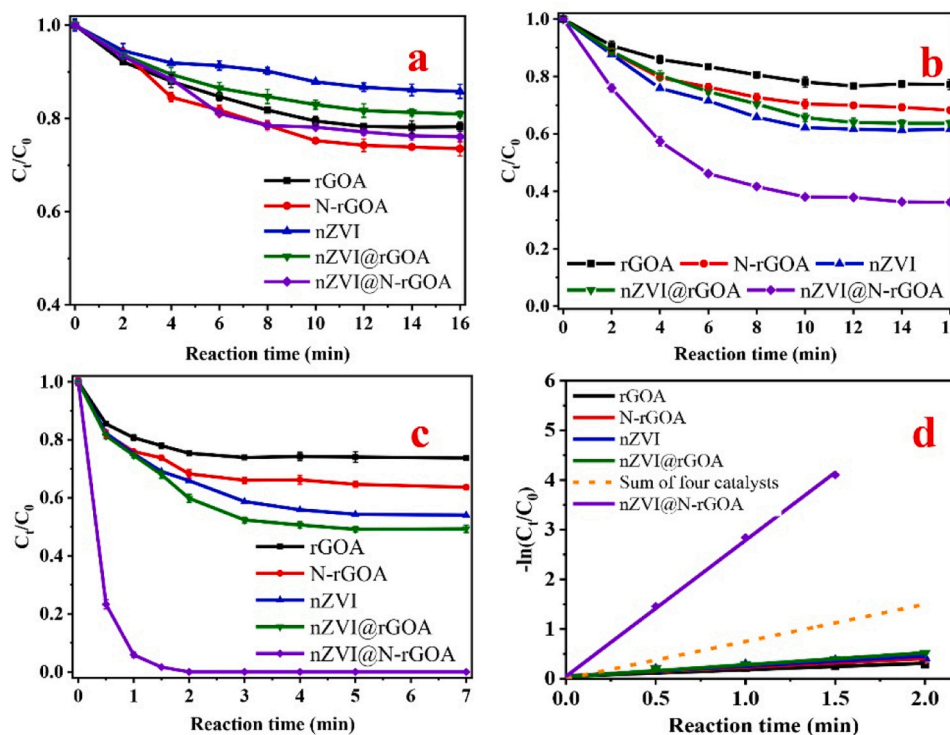


Fig. 3. IMI removal profiles of different catalysts at room temperature (a), traditional heating treatment (b) and MW irradiation (c); fitted removal kinetic curves for the MW-assisted catalytic systems (d).

amount of the catalyst [36]. These results suggested that nZVI@N-rGOA/MW removed IMI more efficiently than the other four catalyst/MW systems.

The IMI removal efficiencies of the catalyst/MW systems, especially nZVI@N-rGOA/MW, were all significantly greater than those seen at room temperature or with heating in an oil bath. MW irradiation without a catalyst did not remove the IMI from solution by volatilisation (data not shown in this study), which was attributed to the low volatility of IMI [37]. Furthermore, the kinetics for the removal of IMI under different reaction conditions, as shown in Fig. 3a-c, illustrated that MW irradiation was superior to the oil bath at the same reaction temperature (90 °C). Furthermore, the HPLC (high-performance liquid chromatography) fingerprint spectrum at 254 nm (Fig. S6) seen for IMI during the degradation process revealed that nZVI@N-rGOA/MW efficiently degraded IMI via oxidation/reduction reactions caused by electrons, holes and ROS, while the nZVI@N-rGOA catalyst only reduced the IMI with nZVI during oil bath heating, as discussed in Text S5 of the SI. In addition, our study suggested that nZVI@N-rGOA, which showed the greatest IMI removal efficiency under MW radiation, required less energy during the heating and holding process than other synthetic materials, even with similar heating programs (Fig. 4). This indicated that nZVI@N-rGOA was more effective in transforming the MW energy into heat via the intrinsic dielectric and conduction mechanisms of N-rGOA. This was consistent with a previous study conducted by Sun et al., who showed that porous biochar heated with MW irradiation consumed less energy than that heated with an oil bath and achieved greater 2,4-D removal [9]. Furthermore, the monitored temperature curves showed more overshooting (~ 7 °C) after ramping of the nZVI@N-rGOA/MW system compared with the other catalyst/MW systems. This confirmed that nZVI@N-rGOA efficiently adsorbed the MW energy and induced localized overheated “hot spots” via intrinsic dielectric and conduction loss heating by N-rGOA and eddy current loss heating by nZVI, thus enhancing IMI removal from the aqueous solution. This was confirmed by the decreased TOC in the MW-assisted catalytic system (Fig. S7). Thus, the carbon and iron matrices of nZVI@N-rGOA absorbed more MW energy and more efficiently converted it into heat.

Moreover, MW irradiation of nZVI@rGOA provided a higher IMI removal rate (50.7%) than oil bath heating (37.9%), both of which were better than the room-temperature treatment (19.1%) (Fig. 3b-c). Moreover, nZVI@N-rGOA exhibited a markedly outstanding

performance in IMI removal with MW irradiation (nearly 100%). This result suggests that nZVI@rGOA and nZVI@N-rGOA exhibited different sensitivities to MW irradiation. It is well established that the MW-absorption capabilities of materials (e.g., carbon material, iron oxides) are related to the magnetic/dielectric/conduction loss factors, which usually depend on the bonding states of the constituent atoms and the microstructure of the material [38]. As described in Section 3.2, the nZVI@N-rGOA had a 3D pomegranate-like multicompartment structure consisting of wrinkled flaky reticular N-rGOA walls with multiple reflections and scattering of incident MW, great dielectric and conduction losses of N-rGOA and eddy current losses of nZVI, which provided a higher MW-absorption capacity, stronger thermal effects and a better catalytic performance than nZVI@rGOA (Figs. 1–2). To clarify the interactions between the N forms in nZVI@N-rGOA and their effects on catalytic IMI degradation, four nZVI@N-rGOA catalysts with various dopants (e.g., melamine, urea, sodium dicyandiamide and cyanoacetamide) were prepared and used to degrade IMI with MW irradiation (Fig. S8a-e). The results showed that the IMI removal efficiencies were positively correlated with the pyridinic N content in nZVI@N-rGOA (Fig. 8f; $r = 0.965$; $p = 0.035$), and nZVI@N-rGOA doped with melamine showed the greatest IMI removal efficiency (Fig. 8e). This suggested that pyridinic N played a vital role in the catalytic performance of nZVI@N-rGOA under MW irradiation. Additionally, the capacities of the MW-absorbing materials for adsorption of organic pollutants was a vital factor in MW-assisted catalytic degradation of pollutants [9]. The strong adsorption of IMI by nZVI@N-rGOA (Fig. S9), which resulted from the hydrophobicity of N-rGOA (Fig. 3a and S4), facilitated mass transfer and IMI capture and the formation of active centres for IMI degradation during MW irradiation.

3.4. Reaction mechanism of nZVI@N-rGOA/MW

3.4.1. Identification and contributions of active species

The efficient removal of IMI by nZVI@N-rGOA/MW can be ascribed to direct reduction via electron trapping and oxidation by active species generated from “hot spots” in the catalyst/MW system [39,40]. A quenching test was conducted to identify the presence and contributions of the active species (e.g., ROS, electrons, and holes). As shown in Fig. 5a, compared with the 99.1% removal rate seen in the absence of scavengers, *p*-BQ reduced the amount of IMI removed to 6.9%; however,

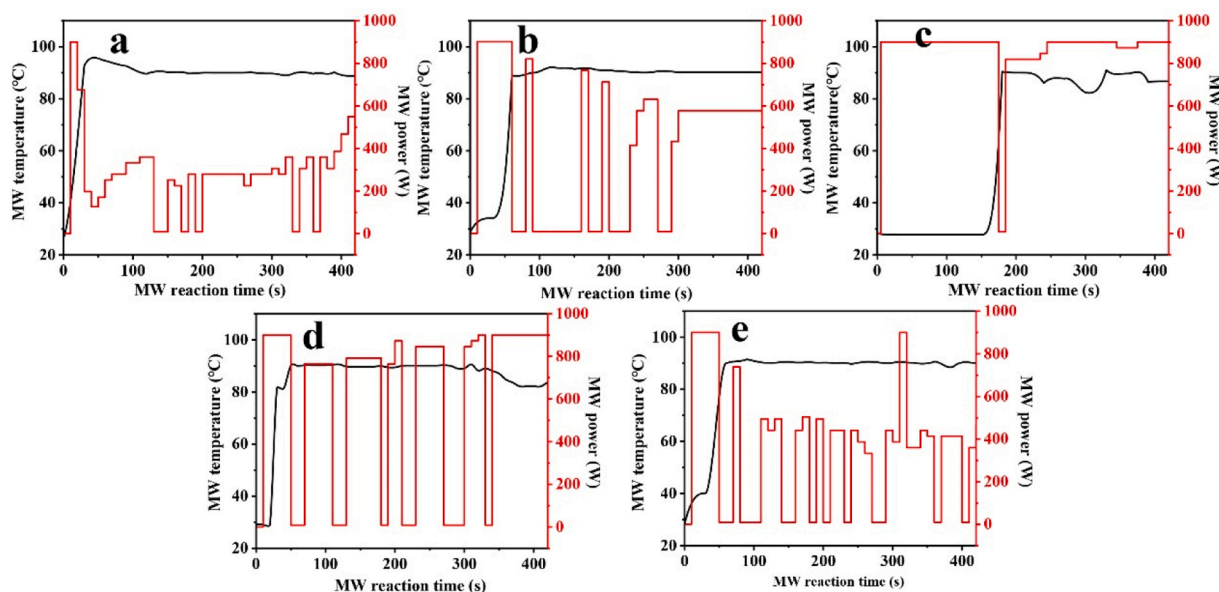


Fig. 4. Water temperature and MW power curves for the MW-assisted systems containing nZVI@N-rGOA (a), nZVI@rGOA (b), nZVI (c), rGOA (d) and N-rGOA (e). (MW parameters: 900 W power, maximum temperature of 90 °C for the catalytic suspension, which was controlled by the MW reactor).

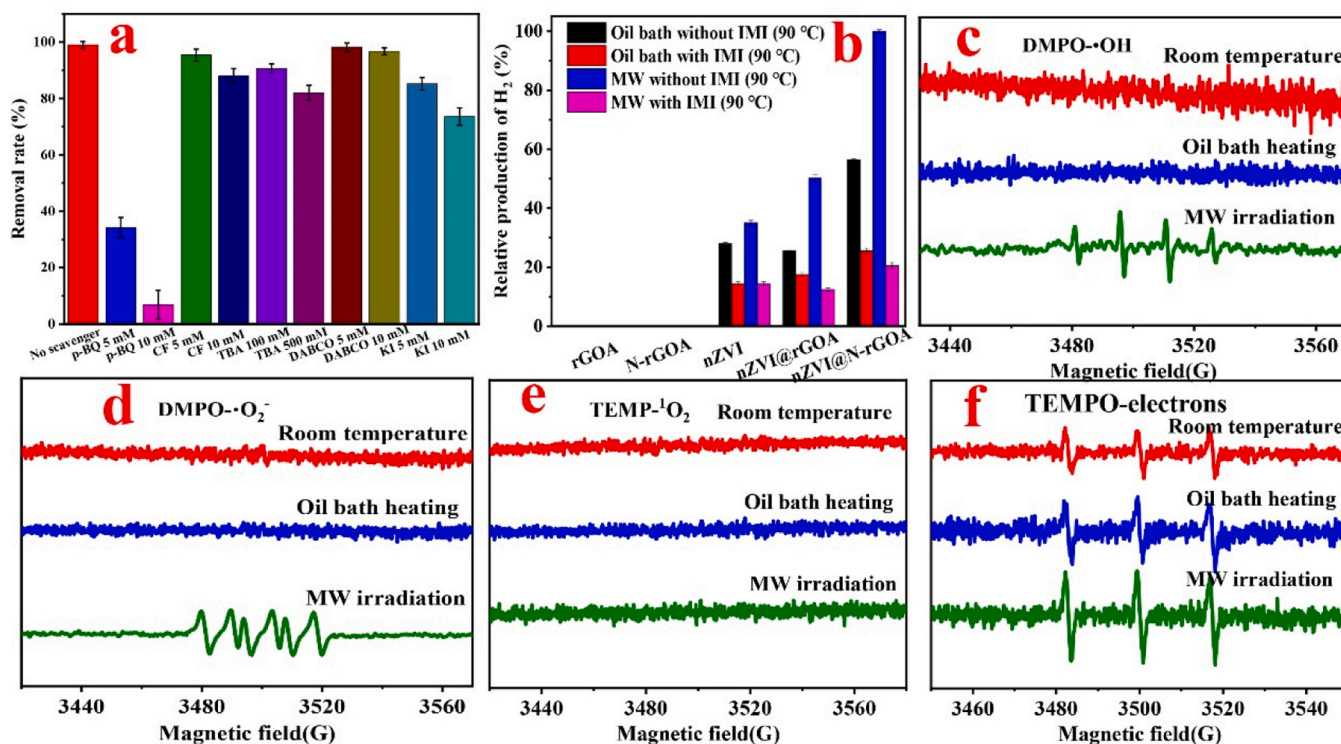


Fig. 5. Influence of various scavengers on the IMI removal efficiency of the nZVI@N-rGOA/MW system (a), relative H₂ production from different MW-assisted systems (b), and EPR spectra of DMPO-•OH (c), DMPO-•O₂⁻ (d), TEMP-¹O₂ (e) and TEMPO-electrons (f) (reaction conditions: catalyst content = 0.5 g/L, DMPO = TEMP = TEMPO = 0.15 M, reaction time = 1.5 min).

CF, TBA and KI only slightly reduced the amounts of IMI removed to 88.1%, 82.1% and 73.6%, respectively, while the DABCO had no effect (96.7%). This suggested that electrons, holes (h^+), •OH and •O₂⁻, and not just ¹O₂, were involved in IMI degradation. However, p-BQ addition led to a more dramatic decline in the IMI removal rate than CF, TBA and KI addition, indicating that electrons played a much more important role than •OH, •O₂⁻ and h^+ . Notably, among these scavengers, only p-BQ showed a substantial effect on IMI removal under oil bath and room temperature conditions, suggesting that only direct reduction of IMI by ZVI was involved (Fig. S6). Because the reductive degradation of IMI was incomplete, catalytic oxidation and mineralization of IMI caused by nZVI@N-rGOA/MW was recommended. A previous study showed that water and organic pollutants competing for electrons from nZVI to produce H₂ inhibited pollutant reduction [41]. H₂ production was monitored for various catalytic systems with or without IMI and with either MW irradiation or oil bath heating, and a greater electron utilization rate was seen for nZVI@N-rGOA/MW subjected to MW irradiation as opposed to oil bath heating (Fig. 5b). This was because the MW-assisted N-rGOA catalyst induced dielectric/conduction/magnetic loss heating around the nZVI, the rapid rise in temperature caused spalling of the iron oxides, and the newly exposed Fe⁰ donated the electrons for IMI degradation [42]. These results confirmed that the active species (except electrons) were only generated by MW irradiation, not during oil bath heating or at room temperature. Moreover, EPR studies were used to verify the generation of ROS and electrons by nZVI@N-rGOA/MW (Fig. 5c-f). Obvious signals for DMPO-•OH, DMPO-•O₂⁻ and TEMP-electrons were observed in the nZVI@N-rGOA/MW system, consistent with the results of the quenching experiment. However, the presence of O₂ had very little impact on IMI degradation (Fig. S10), suggesting that the reactions between O₂ and •OH and electrons made negligible contributions. This confirmed the trivial contribution of •O₂⁻ to IMI degradation seen in the quenching study. These results clearly demonstrated that electrons, holes, •OH and •O₂⁻ all contributed to IMI degradation in the nZVI@N-rGOA/MW

system, and the electrons, holes and •OH played dominant roles.

After use in the MW-assisted catalytic reaction, new peaks appeared at 30–35° and 62.85° in the XRD pattern for nZVI@N-rGOA, and these corresponded to FeO, γ -Fe₂O₃ and Fe₃O₄ (Fig. 6a) [28]. This meant that the nZVI or Fe(II) oxides were oxidized to FeO, γ -Fe₂O₃ and Fe₃O₄ during MW-assisted catalytic degradation of IMI. The secondary minerals FeO, Fe₂O₃ and Fe₃O₄ exhibited great dielectric loss factors and strong MW-adsorbing capacities [29,30], which generated heat via dielectric and conduction losses from “hot spots”, and various active species were formed via induced localized surface plasmon resonance (LSPR) generation. In addition, cracked and popcorn-like iron-containing particles were observed in the SEM images of nZVI@N-rGOA (Fig. 6b-c), which may have been due to spalling of the outer iron oxides caused by the high temperature “hot spots”. The spalling process promoted sustained exposure of the internal Fe⁰.

3.4.2. Reaction mechanism

Based on the experimental results and analyses provided above, a MW-driven reaction mechanism is proposed for the superior catalytic performance of nZVI@N-rGOA. It was noted that nZVI@N-rGOA has a 3D pomegranate-like multicompartiment structure consisting of wrinkled reticular walls with abundant open pores, and it exhibits multiple reflections and scattering of incident MW, which were prevented from escaping the nZVI@N-rGOA. Some of the entering MWs were adsorbed and transformed into heat energy to form “hot spots” via intrinsic dielectric and conduction losses of N-rGOA, and the rest produced LSPR that generated electrons (e^-) and holes (h^+) via eddy current losses of nZVI. N-rGOA markedly improved the MW-harvesting capability of the nZVI, and the pyridinic N sites and micromorphology of the nZVI@N-rGOA played vital roles in the MW-assisted catalysis. Our results showed that the iron in nZVI@N-rGOA comprised Fe⁰ and iron oxides. The iron oxides caused passivation of the nZVI and made it difficult to reduce the IMI directly by electron transfer. In addition to enhancing the catalytic performance of the Fe⁰, physical heating was thought to cause

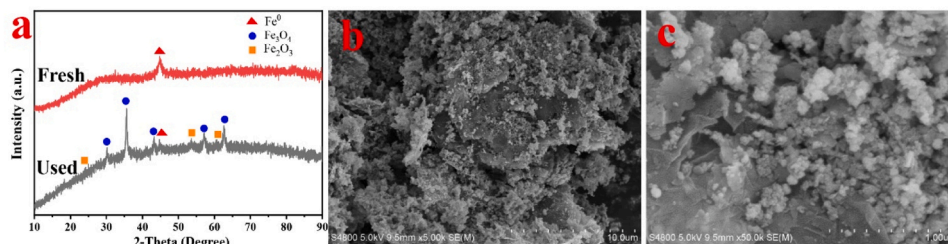


Fig. 6. XRD patterns (a) and SEM images (b and c) of used nZVI@N-rGOA.

spalling of the iron oxides and sustained exposure of the Fe^0 [42]. In this study, MW irradiation of N-rGOA rapidly caused localized overheating and formed “hot spots” through intrinsic dielectric and conduction losses around the nZVI, and the rapid temperature rise caused spalling of the iron oxides. The newly exposed Fe^0 donated electrons to IMI via LSPR and generated Fe^{2+} (Eq. (1)), which was then oxidized to Fe^{3+} or formed Fe_3O_4 , Fe_2O_3 and FeO (Eq. (2)). The high dielectric energy of the generated iron oxides caused efficient separation of the electrons and h^+ under MW irradiation (Eq. (3)). Then, the h^+ and electrons reacted with H_2O , OH^- and O_2 in the water medium to form strongly oxidizing $\bullet\text{OH}$ and $\bullet\text{O}_2^-$ (Eqs. (4)–(6)). Furthermore, the “hot spots” caused by the pyridinic N sites, Fe_3O_4 , Fe_2O_3 and FeO converted the surrounding H_2O into $\bullet\text{OH}$ and $\bullet\text{H}$ through intrinsic dielectric and conduction losses and LSPR (Eq. (7)) [43,44]. Then, the $\bullet\text{H}$ reacted with O_2 in the water to form $\bullet\text{O}_2^-$ (Eq. (8)). These reactive species (e.g., $\bullet\text{OH}$, electrons, holes) with strong reduction and oxidation capacities degraded the IMI into low-molecular-weight intermediates and finally mineralized it to CO_2 and H_2O (Test S5 and Fig. S11). Possible reaction mechanisms for IMI removal by nZVI@N-rGOA/MW are shown in Fig. 7. Additionally, the open pomegranate-like multicompartiment structure of nZVI@N-rGOA provided a large SSA and free reaction cavities and facilitated mass transfer of the reactants as well as contact with the active nZVI. The MW-assisted catalyst may have relied heavily on the LSPR induced by the eddy current losses and 3D porous structure of the catalyst.



3.5. Effect of the water matrix on IMI degradation

Understanding the effects of solution conditions on the catalytic activity of nZVI@N-rGOA/MW is necessary for practical application. To this end, the effects of simulated water matrixes with different initial pH values, cations (Na^+ , Mg^{2+}), and anions (HCO_3^- , NO_3^- , H_2PO_4^-) on IMI degradation were evaluated (Fig. 8). The results showed that nZVI@N-rGOA/MW tolerated a wide pH range of 3.0–11.0. Significant inhibition was observed at a strongly acidic pH (1.0), but the IMI removal rate remained as high as 82.7% (Fig. 8a). This may have been due to rapid corrosion of the nZVI in the strongly acidic solution [45,46], formation of excess Fe(II) and unproductive consumption of electrons from the ZVI, which would hinder the catalytic performance of the nZVI@N-rGOA. Different concentrations of Na^+ and Mg^{2+} and low concentrations (1–5 mg/L) of HCO_3^- , NO_3^- and H_2PO_4^- only slightly inhibited IMI removal (Fig. 8b-c). However, the IMI removal rate was decreased to 75.3% with a high concentration (10 mM) of NO_3^- , and the inhibitory effect was greater than those of HCO_3^- (87.4%) and NO_3^- (83.4%). NO_3^- can be directly reduced by nZVI [47], and it can compete

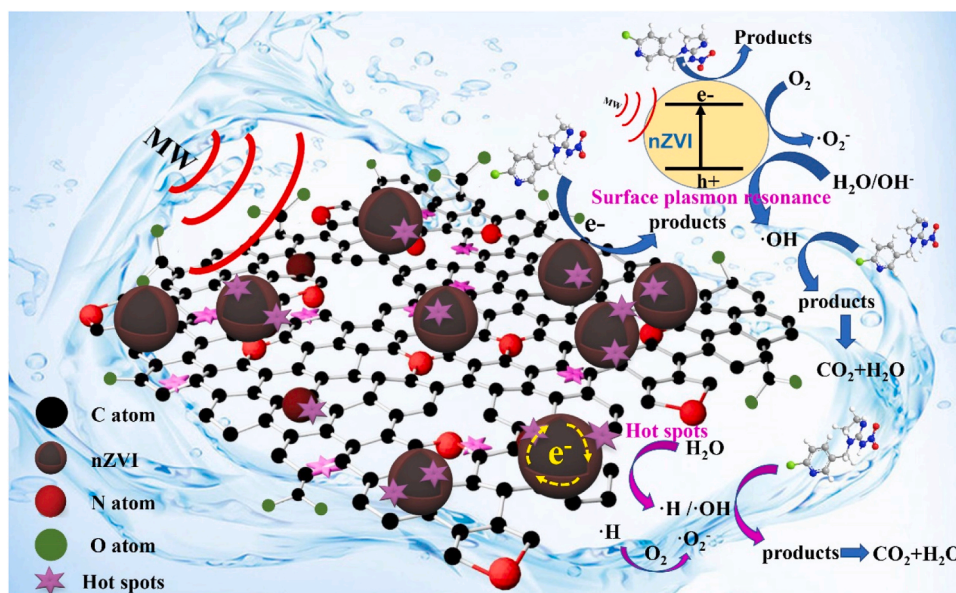


Fig. 7. Proposed mechanism for IMI removal by nZVI@N-rGOA/MW.

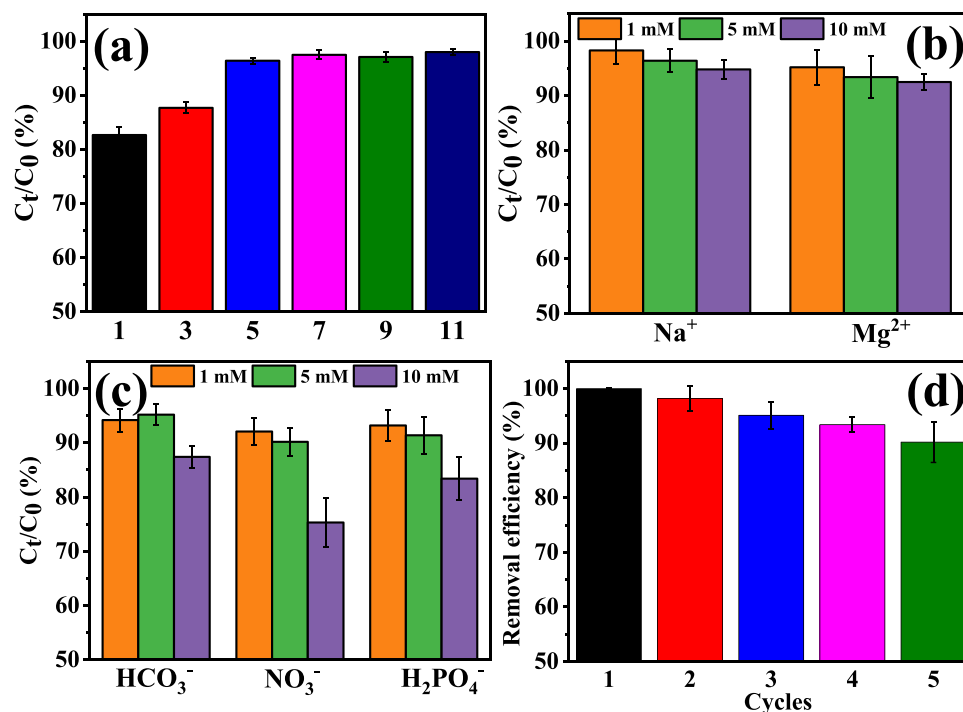


Fig. 8. Influence of pH (a), cations (b), and anions (c) on IMI degradation and five IMI degradation cycles (d) in practical wastewater with MW-assisted nZVI@N-rGOA.

with IMI for active sites on the nZVI@N-rGOA surface as well as change the corrosion potential of the nZVI and form a thermodynamically stable oxide layer [48] that hinders electron transfer from the interior to the surface of the nZVI. Previous studies have also shown that HCO_3^- and $H_2PO_4^-$ form complexes or precipitates with Fe(II) and Fe(III) (passivation layer) on the nZVI surface, which makes the nZVI unavailable for subsequent IMI degradation. Moreover, anions can be activated by free radicals (e.g., $\bullet OH$) to produce the corresponding radical anions, such as Cl^{\bullet} , NO_3^{\bullet} , and HCO_3^{\bullet} [49,50]. However, the generated free radicals have low oxidation potentials and are unable to oxidize organic pollutants, which leads to unproductive consumption of the catalyst [51]. This analysis could explain the slightly decreased IMI removal rates for nZVI@N-rGOA/MW in the presence of high anion concentrations. Thus, the rGOA-nZVI/MW proposed in this study could adapt to a wide pH range and the cations and anions used in IMI removal, confirming the remarkable superiority of rGOA-nZVI/MW for practical application in complicated scenarios.

3.6. Recycling of nZVI@N-rGOA in practical wastewater

The stability and activity of MW-assisted nZVI@N-rGOA was evaluated with five cycles of IMI removal from pesticide plant wastewater with an IMI concentration of 152.6 mg/L. As shown in Fig. 8d, the IMI removal rates declined slightly with increasing numbers of cycles, and 90.2% of the IMI in actual wastewater was removed by nZVI@N-rGOA/MW after five cycles. In addition, the XRD results for nZVI@N-rGOA showed that the ZVI was gradually corroded and transformed into Fe_2O_3 , Fe_3O_4 and FeO by MW irradiation (Fig. 6b-c). However, the amount of Fe leached in the reaction system was very low (Table S3; less than 0.1% of that in nZVI@N-rGOA) during each use cycle. This suggested that the Fe in nZVI@N-rGOA was rather stable, which was ascribed to the strong Fe(II) and Fe(III) adsorption capacities of N-rGOA, which strongly anchored the iron on the N-rGOA carrier [18,19]. The low Fe leaching rate also meant that the catalytic reaction did not induce secondary pollution of the water body. Moreover, the anchored iron on N-rGOA could be regenerated into ZVI by liquid-phase reduction and

used for the next degradation reaction, since nZVI@N-rGOA exhibited excellent stability and recyclability in MW-assisted wastewater treatments.

4. Conclusions

A novel nZVI@N-rGOA composite was successfully synthesized and used as an MW-assisted catalyst to remove organic pollutants from wastewater. The systematic characterization data clearly showed a well-designed 3D open pomegranate-like multicompartiment structure consisting of wrinkled flaky reticular N-rGOA walls and embedded nZVI particles in the nZVI@N-rGOA composite, which resulted in efficient MW capture, mass transfer of the pollutants, high magnetism for easy separation, and highly active nZVI reaction sites, all of which led to excellent catalytic activity, stability and recyclability in MW-assisted catalytic degradation of IMI. Notably, positive coupling of nZVI and N-rGOA was observed during the MW-assisted catalytic removal of IMI, and the nZVI@N-rGOA/MW catalyst increased the IMI removal rate by more than a factor of 10 over those seen for nZVI/MW, nZVI@rGOA/MW and conventional heat treatments. The “hot spots” caused by the intrinsic dielectric and conduction losses and the LSPR caused by the eddy current loss of nZVI both generated the electrons, holes and $\bullet OH$ needed for catalytic oxidation/reduction of IMI. More interestingly, the pyridinic N sites and micromorphology of the nZVI@N-rGOA played vital roles in the MW-assisted catalysis. Above all, the nZVI@N-rGOA catalyst exhibited ample potential for use in remediation of water environments. This work probed the catalytic mechanism and revealed that a customized design of the structure and components of the iron-carbon composite catalysts optimized MW adsorption and the magnetic and dielectric loss factors, and the resulting strong catalytic activity provided a novel and promising strategy with which to remove organic pollutants from wastewater.

CRedit authorship contribution statement

Peng Zhang: Methodology, Investigation, Writing – review & editing

Funding acquisition; **Xingying Meng**, **Mingyi Fan** and **Sai Wu**: Methodology, Investigation, writing – original draft; **Xiaofu Shang**, **Cuiping Wang** and **Hanzhong Jia**: Methodology Writing – review & editing; **Hongwen Sun**: Writing – review & editing funding acquisition.

Declaration of Competing Interest

The authors declare that they have no known competing financial interests or personal relationships that could have appeared to influence the work reported in this paper.

Data availability

Data will be made available on request.

Acknowledgements

This work was supported by the National Key R&D Program of China (No. 2018YFC1802001), the Science and Technology Major Project of Tianjin (No. 22YFZCSN00050), the Special Fund for Technology Innovation Guidance of Tianjin (No. 21YDTPJC00270), the Key R&D Program of Shandong Province (No. 2021CXGC011206), and the Ministry of Education of China (No. T2017002).

Appendix A. Supporting information

Supplementary data associated with this article can be found in the online version at [doi:10.1016/j.apcatb.2023.123258](https://doi.org/10.1016/j.apcatb.2023.123258).

References

- N. Liu, X. Jin, C. Feng, Z. Wang, F. Wu, A.C. Johnson, H. Xiao, H. Hollert, J. P. Giesy, Ecological risk assessment of fifty pharmaceuticals and personal care products (PPCPs) in Chinese surface waters: a proposed multiple-level system, *Environ. Int.* 136 (2020), 105454, <https://doi.org/10.1016/j.envint.2019.105454>.
- B.S. Rathi, P.S. Kumar, D.N. Vo, Critical review on hazardous pollutants in water environment: occurrence, monitoring, fate, removal technologies and risk assessment, *Sci. Total Environ.* 797 (2021), 149134, <https://doi.org/10.1016/j.scitotenv.2021.149134>.
- S.F. Ahmed, M. Mofijur, S. Nuzhat, A.T. Chowdhury, N. Rafa, M.A. Uddin, A. Inayat, T.M.I. Mahlia, H.C. Ong, W.Y. Chia, P.L. Show, Recent developments in physical, biological, chemical, and hybrid treatment techniques for removing emerging contaminants from wastewater, *J. Hazard. Mater.* 416 (2021), 125912, <https://doi.org/10.1016/j.jhazmat.2021.125912>.
- R. Shu, J. Zhang, C. Guo, Y. Wu, Z. Wan, J. Shi, Y. Liu, M. Zheng, Facile synthesis of nitrogen-doped reduced graphene oxide/nickel-zinc ferrite composites as high-performance microwave absorbers in the X-band, *Chem. Eng. J.* 384 (2020), 123266, <https://doi.org/10.1016/j.cej.2019.123266>.
- H. Xia, C. Li, G. Yang, Z. Shi, C. Jin, W. He, J. Xu, G. Li, A review of microwave-assisted advanced oxidation processes for wastewater treatment, *Chemosphere* 287 (2022), 131981, <https://doi.org/10.1016/j.chemosphere.2021.131981>.
- K. Wang, Y. Chen, H. Li, B. Chen, K. Zeng, Y. Chen, H. Chen, Q. Liu, H. Liu, Fe/N-codoped hollow carbonaceous nanospheres anchored on reduced graphene oxide for microwave absorption, *ACS Appl. Nano Mater.* 2 (2019) 8063–8074, <https://doi.org/10.1021/acsanm.9b02192>.
- Y. Gao, D. Zou, Efficient degradation of levofloxacin by a microwave–3D ZnCo₂O₄/activated persulfate process: effects, degradation intermediates, and acute toxicity, *Chem. Eng. J.* 393 (2020), <https://doi.org/10.1016/j.cej.2020.124795>.
- E. Calcio Gaudino, G. Cravotto, M. Manzoli, S. Tabasso, From waste biomass to chemicals and energy via microwave-assisted processes, *Green. Chem.* 21 (2019) 1202–1235, <https://doi.org/10.1039/c8gc03908a>.
- Y. Sun, I.K.M. Yu, D.C.W. Tsang, J. Fan, J.H. Clark, G. Luo, S. Zhang, E. Khan, N.J. D. Graham, Tailored design of graphitic biochar for high-efficiency and chemical-free microwave-assisted removal of refractory organic contaminants, *Chem. Eng. J.* 398 (2020), 125505, <https://doi.org/10.1016/j.cej.2020.125505>.
- L. Guo, Q.-D. An, Z.-Y. Xiao, S.-R. Zhai, L. Cui, Inherent N-doped honeycomb-like carbon/Fe₃O₄ composites with versatility for efficient microwave absorption and wastewater treatment, *ACS Sustain. Chem. Eng.* 7 (2019) 9237–9248, <https://doi.org/10.1021/acssuschemeng.9b00067>.
- A.L. Garcia-Costa, J.A. Zazo, J.J. Rodriguez, J.A. Casas, Microwave-assisted catalytic wet peroxide oxidation. Comparison of Fe catalysts supported on activated carbon and gamma-alumina, *Appl. Catal. B-Environ.* 218 (2017) 637–642, <https://doi.org/10.1016/j.apcatb.2017.06.058>.
- C.J. Jou, Degradation of pentachlorophenol with zero-valence iron coupled with microwave energy, *J. Hazard. Mater.* 152 (2008) 699–702, <https://doi.org/10.1016/j.jhazmat.2007.07.036>.
- A. Zhang, Z. Gu, W. Chen, Q. Li, Degradation of leachate from a semi-anaerobic aged refuse biofilter by the ZVI/H₂O₂ process coupled with microwave irradiation: optimization, organics transformation, and reaction mechanisms, *Environ. Sci. Technol.* 4 (2018) 1695–1709, <https://doi.org/10.1039/c8ew00469b>.
- Y. Mao, Z. Xi, W. Wang, C. Ma, Q. Yue, Kinetics of solvent blue and reactive yellow removal using microwave radiation in combination with nanoscale zero-valent iron, *J. Environ. Sci.* 30 (2015) 164–172, <https://doi.org/10.1016/j.jes.2014.09.030>.
- X. Liu, D. Xu, Q. Wang, L. Zhang, Fabrication of 3D hierarchical byttneria asperalike Ni@graphitic carbon yolk-shell microspheres as bifunctional catalysts for ultraefficient oxidation/reduction of organic contaminants, *Small* (2018) 1803188, <https://doi.org/10.1002/sml.201803188>.
- L.P. Lingamdinne, J.R. Koduru, R.R. Karri, A comprehensive review of applications of magnetic graphene oxide based nanocomposites for sustainable water purification, *J. Environ. Manag.* 231 (2019) 622–634, <https://doi.org/10.1016/j.jenvman.2018.10.063>.
- X. Zhang, X. Zhang, H. Yuan, K. Li, Q. Ouyang, C. Zhu, S. Zhang, Y. Chen, CoNi nanoparticles encapsulated by nitrogen-doped carbon nanotube arrays on reduced graphene oxide sheets for electromagnetic wave absorption, *Chem. Eng. J.* 383 (2020), 123208, <https://doi.org/10.1016/j.cej.2019.123208>.
- M. Fan, P. Zhang, C. Wang, J. Tang, H. Sun, Tailored design of three-dimensional rGOA-nZVI catalyst as an activator of persulfate for degradation of organophosphorus pesticides, *J. Hazard. Mater.* 428 (2022), 128254, <https://doi.org/10.1016/j.jhazmat.2022.128254>.
- P. Huang, P. Zhang, C. Wang, J. Tang, H. Sun, Enhancement of persulfate activation by Fe-biochar composites: synergism of Fe and N-doped biochar, *Appl. Catal. B-Environ.* 303 (2022), 120926, <https://doi.org/10.1016/j.apcatb.2021.120926>.
- T. Yao, Y. Qi, Y. Mei, Y. Yang, R. Aleisa, X. Tong, J. Wu, One-step preparation of reduced graphene oxide aerogel loaded with mesoporous copper ferrite nanocubes: a highly efficient catalyst in microwave-assisted Fenton reaction, *J. Hazard. Mater.* 378 (2019), 120712, <https://doi.org/10.1016/j.jhazmat.2019.05.105>.
- X. Zhang, J. Xu, H. Yuan, S. Zhang, Q. Ouyang, C. Zhu, X. Zhang, Y. Chen, Large-scale synthesis of three-dimensional reduced graphene oxide/nitrogen-doped carbon nanotube heteronanostructures as highly efficient electromagnetic wave absorbing materials, *ACS Appl. Mater. Interfaces* 11 (2019) 39100–39108, <https://doi.org/10.1021/acsami.9b13751>.
- R. Wei, P. Wang, G. Zhang, N. Wang, T. Zheng, Microwave-responsive catalysts for wastewater treatment: a review, *Chem. Eng. J.* 382 (2020), <https://doi.org/10.1016/j.cej.2019.122781>.
- M. Gu, U. Farooq, S. Lu, X. Zhang, Z. Qiu, Q. Sui, Degradation of trichloroethylene in aqueous solution by rGO supported nZVI catalyst under several oxidic environments, *J. Hazard. Mater.* 349 (2018) 35–44, <https://doi.org/10.1016/j.jhazmat.2018.01.037>.
- J. Li, Q. Lin, H. Luo, H. Fu, L. Wu, Y. Chen, Y. Ma, The effect of nanoscale zero-valent iron-loaded N-doped biochar on the generation of free radicals and nonradicals by peroxydisulfate activation, *J. Water Process Eng.* 47 (2022), 102681, <https://doi.org/10.1016/j.jwpe.2022.102681>.
- I. Hussain, M. Li, Y. Zhang, Y. Li, S. Huang, X. Du, G. Liu, W. Hayat, N. Anwar, Insights into the mechanism of persulfate activation with nZVI/BC nanocomposite for the degradation of nonylphenol, *Chem. Eng. J.* 311 (2017) 163–172, <https://doi.org/10.1016/j.cej.2016.11.085>.
- X. Gao, Y. Wang, Q. Wang, X. Wu, W. Zhang, C. Luo, Facile synthesis of hollow cube-like ZnSnO₃ wrapped by nitrogen-doped graphene: as a high-performance and enhanced synergistic microwave absorber, *J. Magn. Magn. Mater.* 486 (2019), <https://doi.org/10.1016/j.jmmm.2019.165251>.
- X. Wang, P. Liu, M. Fu, J. Ma, P. Ning, Novel sequential process for enhanced dye synergistic degradation based on nano zero-valent iron and potassium permanganate, *Chemosphere* 155 (2016) 39–47, <https://doi.org/10.1016/j.chemosphere.2016.04.022>.
- Y. Chen, Z. Lin, R. Hao, H. Xu, C. Huang, Rapid adsorption and reductive degradation of naphtholgreen B from aqueous solution by polypyrrole/attapulgite composites supported nanoscale zero-valent iron, *J. Hazard. Mater.* 371 (2019) 8–17, <https://doi.org/10.1016/j.jhazmat.2019.02.096>.
- Z. Li, X. Li, Y. Zong, G. Tan, Y. Sun, Y. Lan, M. He, Z. Ren, X. Zheng, Solvothermal synthesis of nitrogen-doped graphene decorated by superparamagnetic Fe₃O₄ nanoparticles and their applications as enhanced synergistic microwave absorbers, *Carbon* 115 (2017) 493–502, <https://doi.org/10.1016/j.carbon.2017.01.036>.
- P. Wang, J. Zhang, G. Wang, B. Duan, D. He, T. Wang, F. Li, Synthesis and characterization of MoS₂/Fe@Fe₃O₄ nanocomposites exhibiting enhanced microwave absorption performance at normal and oblique incidences, *J. Mater. Sci. Technol.* 35 (2019) 1931–1939, <https://doi.org/10.1016/j.jmst.2019.05.021>.
- R. Qiang, Y. Du, Y. Wang, N. Wang, C. Tian, J. Ma, P. Xu, X. Han, Rational design of yolk-shell C@C microspheres for the effective enhancement in microwave absorption, *Carbon* 98 (2016) 599–606, <https://doi.org/10.1016/j.carbon.2015.11.054>.
- P. Liu, Y. Zhang, J. Yan, Y. Huang, L. Xia, Z. Guang, Synthesis of lightweight N-doped graphene foams with open reticular structure for high-efficiency electromagnetic wave absorption, *Chem. Eng. J.* 368 (2019) 285–298, <https://doi.org/10.1016/j.cej.2019.02.193>.
- X. Qiu, L. Wang, H. Zhu, Y. Guan, Q. Zhang, Lightweight and efficient microwave absorbing materials based on walnut shell-derived nano-porous carbon, *Nanoscale* 9 (2017) 7408–7418, <https://doi.org/10.1039/c7nr02628e>.
- P. Zhang, H. Sun, C. Ren, L. Min, H. Zhang, Sorption mechanisms of neonicotinoids on biochars and the impact of deashing treatments on biochar structure and

- neonicotinoids sorption, *Environ. Pollut.* 234 (2018) 812–820, <https://doi.org/10.1016/j.envpol.2017.12.013>.
- [35] X. Zhou, Y. Tian, X. Liu, L. Huang, Y. Wen, Reduction of imidacloprid by sponge iron and identification of its degradation products, *Water Environ. Res.* 90 (2018) 2049–2055, <https://doi.org/10.2175/106143017X15131012188187>.
- [36] Q. Kan, K. Lu, S. Dong, D. Shen, Q. Huang, Y. Tong, W. Wu, S. Gao, L. Mao, Transformation and removal of imidacloprid mediated by silver ferrite nanoparticle facilitated peroxymonosulfate activation in water: reaction rates, products, and pathways, *Environ. Pollut.* 267 (2020), 115438, <https://doi.org/10.1016/j.envpol.2020.115438>.
- [37] X.Y. Bi, K.L. Yang, On-Line monitoring imidacloprid and thiacloprid in celery juice using quartz crystal microbalance, *Anal. Chem.* 81 (2009) 527–532, <https://doi.org/10.1021/ac801786a>.
- [38] Y. Wang, X. Gao, X. Wu, W. Zhang, Q. Wang, C. Luo, Hierarchical ZnFe_2O_4 @RGO@CuS composite: strong absorption and wide-frequency absorption properties, *Ceram. Int.* 44 (2018) 9816–9822, <https://doi.org/10.1016/j.ceramint.2018.02.220>.
- [39] A. Veksha, P. Pandya, J.M. Hill, The removal of methyl orange from aqueous solution by biochar and activated carbon under microwave irradiation and in the presence of hydrogen peroxide, *J. Environ. Chem. Eng.* 3 (2015) 1452–1458, <https://doi.org/10.1016/j.jece.2015.05.003>.
- [40] Y. Lei, X. Lin, H. Liao, New insights on microwave induced rapid degradation of methyl orange based on the joint reaction with acceleration effect between electron hopping and Fe^{2+} - H_2O_2 reaction of NiFeMnO_4 nanocomposites, *Sep. Purif. Technol.* 192 (2018) 220–229, <https://doi.org/10.1016/j.seppur.2017.09.067>.
- [41] F. He, Z. Li, S. Shi, W. Xu, H. Sheng, Y. Gu, Y. Jiang, B. Xi, Dechlorination of excess trichloroethene by bimetallic and sulfidated nanoscale zero-valent iron, *Environ. Sci. Technol.* 52 (2018) 8627–8637, <https://doi.org/10.1021/acs.est.8b01735>.
- [42] F. He, Y. Yu, W. Wan, L. Liang, Enhanced dechlorination of trichloroethene by sulfidated microscale zero-valent iron under low-frequency AC electromagnetic field, *J. Hazard. Mater.* 423 (2022), 127020, <https://doi.org/10.1016/j.jhazmat.2021.127020>.
- [43] B. Cai, J.F. Feng, Q.Y. Peng, H.F. Zhao, Y.C. Miao, H. Pan, Super-fast degradation of high concentration methyl orange over bifunctional catalyst $\text{Fe}/\text{Fe}_3\text{C}@C$ with microwave irradiation, *J. Hazard. Mater.* 392 (2020), 122279, <https://doi.org/10.1016/j.jhazmat.2020.122279>.
- [44] K. Xiao, K. Pei, H. Wang, W. Yu, S. Liang, J. Hu, H. Hou, B. Liu, J. Yang, Citric acid assisted Fenton-like process for enhanced dewaterability of waste activated sludge with in-situ generation of hydrogen peroxide, *Water Res.* 140 (2018) 232–242, <https://doi.org/10.1016/j.watres.2018.04.051>.
- [45] D. Silvestri, S. Wacławek, B. Sobel, R. Torres-Mendieta, M. Pawlyta, V.V.T. Padil, J. Filip, M. Černík, Modification of nZVI with a bio-conjugate containing amine and carbonyl functional groups for catalytic activation of persulfate, *Sep. Purif. Technol.* 257 (2021), <https://doi.org/10.1016/j.seppur.2020.117880>.
- [46] E. Xingu-Contreras, G. García-Rosales, I. García-Sosa, A. Cabral-Prieto, Degradation of methyl orange using iron nanoparticles with/without support at different conditions, *Microporous Mesoporous Mat.* 292 (2020), <https://doi.org/10.1016/j.micromeso.2019.109782>.
- [47] J. Huang, S. Yi, C. Zheng, I.M.C. Lo, Persulfate activation by natural zeolite supported nanoscale zero-valent iron for trichloroethylene degradation in groundwater, *Sci. Total Environ.* 684 (2019) 351–359, <https://doi.org/10.1016/j.scitotenv.2019.05.331>.
- [48] Q. Lu, S.W. Jeon, L. Gui, R.W. Gillham, Nitrate reduction and its effects on trichloroethylene degradation by granular iron, *Water Res.* 112 (2017) 48–57, <https://doi.org/10.1016/j.watres.2017.01.031>.
- [49] C. Chen, T. Ma, Y. Shang, B. Gao, B. Jin, H. Dan, Q. Li, Q. Yue, Y. Li, Y. Wang, X. Xu, In-situ pyrolysis of enteromorpha as carbocatalyst for catalytic removal of organic contaminants: considering the intrinsic N/Fe in enteromorpha and non-radical reaction, *Appl. Catal. B-Environ.* 250 (2019) 382–395, <https://doi.org/10.1016/j.apcatb.2019.03.048>.
- [50] S. Xiao, M. Cheng, H. Zhong, Z. Liu, Y. Liu, X. Yang, Q. Liang, Iron-mediated activation of persulfate and peroxymonosulfate in both homogeneous and heterogeneous ways: a review, *Chem. Eng. J.* 384 (2020), 123265, <https://doi.org/10.1016/j.cej.2019.123265>.
- [51] L. Wang, X. Lan, W. Peng, Z. Wang, Uncertainty and misinterpretation over identification, quantification and transformation of reactive species generated in catalytic oxidation processes: a review, *J. Hazard. Mater.* 408 (2021), 124436, <https://doi.org/10.1016/j.jhazmat.2020.124436>.